Portable turbulence profilers: from MASS to RINGSS

Andrei Tokovinin[a], Edison Bustos[a], and Rossano Rivera[a]

[a] Cerro Tololo Inter-American Observatory — NSF's NOIRLab, Casilla 603, La Serena, Chile

ABSTRACT

The Ring-Image Next Generation Scintillation Sensor (RINGSS) is a replacement of the popular but obsolete low-resolution MASS turbulence profilers. It uses a cheap CMOS camera on a small 13-cm telescope. Turbulence integrals in 8 layers (including the ground layer) are estimated (hence the total and free-atmosphere seeing), as well as the effective wind speed and the AO time constant. Defocused image of a bright single star is optically transformed into a ring, and movies with 1-ms sampling are analyzed in the same way as in MASS, although the underlying theory is more complex. The RINGSS hardware consists of commercially available parts. The data analysis algorithm (estimation of turbulence profiles from the cubes of ring images) is coded in both IDL and python and is publicly available. The first instrument operates robotically at Cerro Tololo since November 2022. Comparison between RINGSS and other profilers at Cerro Tololo and Paranal is presented.

Keywords: Site testing, turbulence profile, scintillation

1. INTRODUCTION

Small, portable monitors of turbulence profile are needed for testing new prospective sites for night-time astronomy. Combination of the Multi-Aperture Scintillation Sensor (MASS)[7] with the Differential Image Motion Monitor (DIMM) in one instrument[8] has been used for nearly two decades both for site testing (e.g. ref. 14) and for the regular turbulence monitoring at major observatories. However, the MASS instrument employs an obsolete technology (photo-multipliers), and search for its replacement based on solid-state sensors has been undertaken by several teams.[3,5] The Ring-Image Next Generation Scintillation Sensor (RINGSS) is yet another approach presented in ref. 17. Its principle and theory are well covered in the above publication; they will be recalled here only briefly, focusing instead on the instrument, software, and the first results.

RINGSS, like MASS, belongs to the family of single-star turbulence profilers, where dependence of the spatial scale of scintillation on the propagation distance is used to distinguish between near and far layers and to estimate low-resolution turbulence profiles. All single-star profilers use some form of spatial filtering of scintillation patterns (e.g. four concentric annular apertures in MASS) and have common physical limitations enumerated below.

1. The spatial scale of scintillation is governed by the Fresnel radius $r_F = \sqrt{\lambda z}$ for a wavelength λ and a propagation distance z. In the optical, r_F varies between 1.5 cm and 10 cm for z between 0.5 and 20 km. This sets the required spatial sampling.

2. The small spatial scale and the fast wind in the upper atmosphere require a fast temporal sampling. For a wind speed of 20 m/s and an exposure time of 1 ms, the spatial blur is 2 cm, comparable to r_F. The exposure time of 1 ms is a tolerable maximum, but faster acquisition is desirable.

3. The spatial and temporal scales determine the number of photons received from the stars. For a continuous monitoring, stars as faint as magnitude 2 must be used. Such a star gives on the order of 80 photo-electrons per cm^2 in 1 ms (assuming a total quantum efficiency of 0.5 and a spectral bandwidth of 100 nm). So, single-star profilers need fast and low-noise light sensors.

4. The spatial spectrum of scintillation differs from its theoretical weak-turbulence form owing to partial saturation. This effect causes non-negligible biases and should be accounted for.

E-mail: andrei.tokovinin@noirlab.edu

Turbulence near the ground does not produce any scintillation, so measurement of the total seeing is usually based on sensing phase distortions. The strongest wave-front terms, tilts, are corrupted by telescope shake, so the next-strongest effect, curvature, is used in instruments like DIMM, FADE,[16] or a Shack-Hartmann sensor. The differential tilt signal increases approximately in proportion to the baseline, hence to the telescope aperture size D. The number of collected photons $N_{\rm ph}$ is proportional to the sub-aperture area, d^2, while the diffraction-limited size of the spots varies as d^{-1}, so the centroid noise is proportional to d^{-2} (or D^{-2}), and the signal to noise ratio varies as D^{-3}. In fact, the dependence on D is even stronger if we account for the exposure time. There is a severe penalty on the reduction of the aperture size, desirable for cutting down the cost and increasing the portability. Practically, seeing monitors use apertures D between 20 and 35 cm. In the first RINGSS instrument, a challengingly small aperture of $D = 13$ cm is chosen to demonstrate that seeing measurement is still possible using modern light detectors even under excellent conditions (measuring poor seeing is never a problem).

Yet another penalty on the small aperture in a DIMM-like turbulence monitor is the drop of sensitivity owing to propagation, which becomes substantial when $d \sim r_F$. The standard DIMM theory neglects propagation, and this is tolerable only for $d > 10$ cm. Accounting for the propagation requires knowledge of the turbulence profile. This correction is implemented in RINGSS. Another, equivalent way to deal with propagation is chosen in the SHIMM turbulence profiler.[3]

An alternative way of sensing near-ground turbulence consists in converting phase distortions into scintillation by means of the so-called virtual propagation inside the instrument. This idea is realized in the Generalized SCIDAR,[1,6,11] in FASS,[5] and in RINGSS. For a modest virtual propagation distance of ∼0.5 km, the ground layer creates a small-scale scintillation pattern of low amplitude. This signal, however, can still be reliably measured, as shown by simulations and demonstrated in practice. So, RINGSS implements two alternative methods for measuring the total seeing: from the wave-front curvature as in DIMM and from the generalized scintillation. Mutual agreement between those two seeing estimates increases the confidence. Simulations indicate that the scintillation-based seeing estimate is less biased.

Matching the small pixel size of modern detectors (e.g. 2.9 μm in the RINGSS CMOS camera) to the spatial scale of scintillation (∼1 cm) requires a huge optical de-magnification factor of several thousand. While possible in principle, this implies a small field of view and the need for an accurate guiding. To alleviate the problem by increasing the effective pixel size, a CCD with binning to was used in the first incarnation of FASS.[4] Putting the detector in the image plane and recording defocused images solves the problems of pixel size and guiding and, at the same time, implements a virtual propagation for the generalized operation. Sharpening of the ring image in the radial direction, compared to a pure defocus, increases the signal by concentrating the light in a smaller number of pixels. Yet another flavor of scintillation sensors with detection in the image plane employs pupil segmentation by a Shack-Hartmann sensor.[3,10,12,13]

2. THE RINGSS INSTRUMENT

2.1 Operational principle of RINGSS

In a RINGSS instrument, a conic aberration is used to transform stellar image into a ring. The ring is focused in the radial direction, and its distortion allows measurement of the instantaneous low-order aberrations in a DIMM-like manner to evaluate the total seeing. On the other hand, intensity variation along the ring (over the azimuth angle θ) is related to the intensity fluctuations at the entrance annular pupil of the telescope, — scintillation.

In the data processing, each ring image is centered and multiplied by a set of masks defined in polar coordinates. The radial part of each mask isolates the ring pixels from the rest of the image (background). The angular part is proportional to $\cos(m\theta)$ and $\sin(m\theta)$, thus implementing Fourier transform over angular coordinate θ with frequencies from $m = 0$ (integrated flux) to $m_{\max} = 20$. The sine and cosine signals derived from the image cube are processed by computing their variances and covariances with a lag of one frame. The angular power spectrum (APS) $S(m)$ (sum of cosine and sine variances) is corrected for biases (subtract the noise bias, account for the final exposure time and for the saturation), and approximated by $j = 8$ turbulent layers at fixed heights

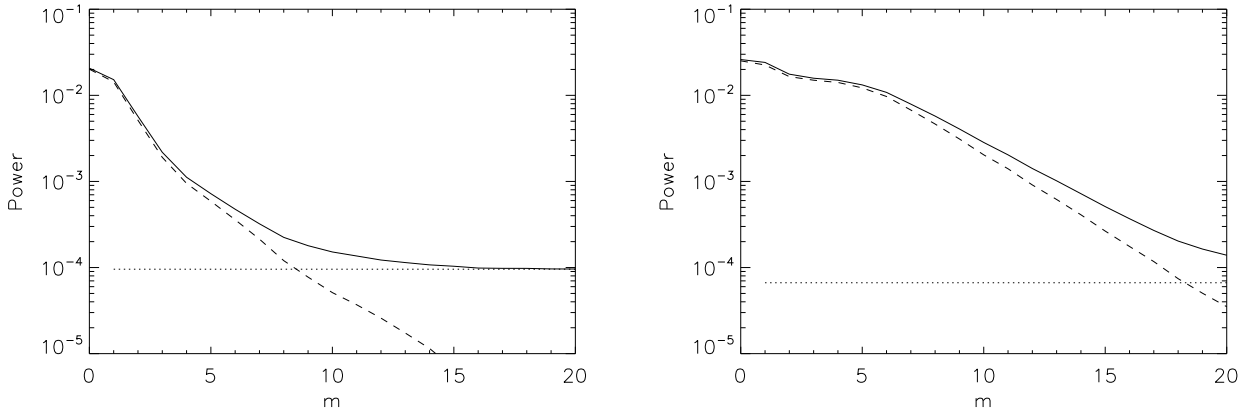

Figure 1. Angular power spectra (full lines) and covariances (dashed lines) recorded at Paranal under excellent seeing (left, 0.33″, 2023-03-05 UT 01:29:39) and poor seeing (right, 2.26″, 2023-03-04 UT 08:12:48). Horizontal dotted lines show the noise level computed from the flux.

above ground:

$$S_m \approx \sum_{j=1}^{8} W_{m,j} J_j, \tag{1}$$

where J_j are turbulence integrals (in $m^{1/3}$) in the layers and $W_{m,j}$ are the weighting functions (WFs), computed for a specific instrument and accounting for its spectral response and the star color. The system of equations (1) is solved by the standard non-negative least squares method to find J_j.

Figure 1 shows examples of the APS recorded at Paranal (averages over 10 cubes). Under the exceptionally good 0.3″ seeing, without turbulence in the ground layer, the scintillation signal at large m is very weak, the APS is dominated by the noise (mostly photon noise from star HR 3685 of $V = 1.69$ magnitude, flux $1.1{\times}10^4$ electrons per frame). The noise estimate (dotted line) accurately matches the APS at $m > 15$. Under poor seeing, illustrated in the right panel, the signal completely dominates over the noise.

For the alternative seeing measurement, the ring is divided into eight 45° sectors and the radius in each sector is computed by multiplication with a suitable mask. The differential radius variations in opposite pairs of sectors are equivalent to four DIMMs working in parallel. They are related to the turbulence profile J_j by a set of WFs that take into account propagation (unlike in a standard DIMM, where a constant response is assumed). The sector variance could be included in (1) as an additional equation. Instead, the turbulence profile deduced from the scintillation is used to find the effective (propagation-weighted) WF for the sector motion and to derive another estimate of the full seeing. A detailed description of the RINGSS method and theory can be found in ref. 17.

The effective (turbulence-weighted) wind speed V_2 is estimated by the method of Kornilov.[9] The input data are the differences Δ_m between the noise-corrected power S_m and the covariance S^1_m with a lag of one frame, at several selected angular frequencies m. The differences are related to the wind speed and the propagation distance by means of the so-called U functions. A suitable linear combination of the U-functions effectively eliminates the distance dependence, so the corresponding linear combination of Δ_m enables estimation of V_2.

2.2 The hardware

The RINGSS instrument in Fig. 2 has been assembled from the commercial components listed in Table 1. The 5-inch Schmidt-Cassegrain telescope is very compact (external tube diameter 150 mm, length 290 mm). Details of its focal reducer and filters are available in the document.* The lenses and filters are mounted in a small barrel that couples detector to the telescope. The pixel scale of ∼ 1.6″ (effective focal length 370 mm) samples well

*http://www.ctio.noirlab.edu/~atokovin/ringss/RINGSS-Celestron.pdf

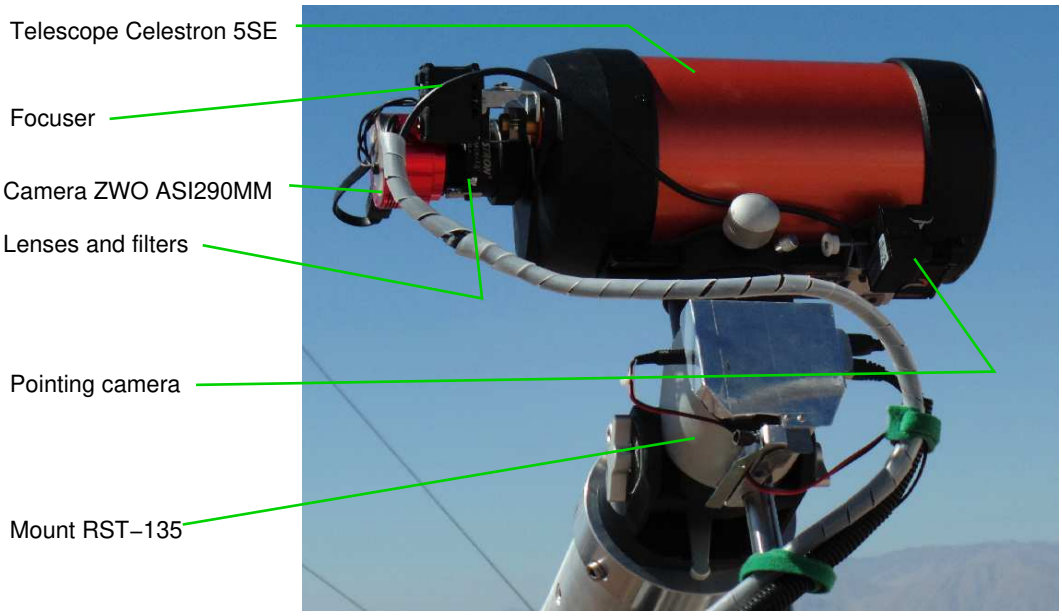

Figure 2. Main components of the RINGSS instrument.

Table 1. Commercial components of the RINGSS turbulence profiler

Item	Model	Vendor
Telescope	Nexstar 5SE, $D = 127$ mm, $F/10$	Celestron
Main camera	ASI 290MM, 1936×1096, 2.9 μm pixel	ZWO
Mount	RST-135	Rainbow Astro
Lenses	#47-919, #47-661	Edmund Optics
Filters	RES0750, FGL455	Thorlabs
Focuser	AX-12A, RS485-USB converter	Dynamixel
Pointing camera	SV305 Pro camera with lens	SVBony
Main computer	NUC	Intel

the diffraction-limited ring width, while the field of view reaches almost 0.5°, facilitating star acquisition in the wide 1024^2 pixel images. The nominal ring radius where the spherical aberration and defocus match each other to produce a conic wave-front is 11 pixels (conjugation distance −460 m). The central obscuration is increased from 50 mm to 63 mm by a mask attached in front of the meniscus.

Images of 48×48 pixels around the center are recorded with an exposure time of 1 ms and 2000 frames per cube. The uncooled CMOS camera ASI290MM is the core component of the instrument. It has been studied by us, confirming the low readout noise (about 1 electron, except in a 0.2% fraction of noisy pixels) and the peak quantum efficiency of 0.8, although the measured spectral response maximum is at 480 nm wavelength, shorter than in the the vendor's curve that peaks at 600 nm. The relation between the gain setting and the actual gain in electrons per ADU is hard-coded in the software for the flux conversion to electrons and noise calculation. The pixel response is so uniform (0.8% rms) that no flat-field correction is applied.

The focus knob of the Celestron works very smoothly without shifting the image (unlike in some other amateur telescopes). This allows us to control and stabilize the focus (maintain constant ring radius) by attaching a small servo motor to the knob.

The most expensive commercial component of our system is the compact mount RST-135. In can work in both equatorial and alt-az modes. This harmonic-drive mount is strong and stiff, over-specified for our small telescope to resist strong wind. Built-in home sensors allow remote initialization after a power cut. After determining the pointing model on several bright stars, the pointed object is always found near the center of the main camera field, so the pointing camera is not used in regular operation, only during the setup.

2.3 Software

The software is a key component of the RINGSS profiler. Image processing, calculation of the WFs, and profile restoration have been coded in IDL and ported to python; both codes and their descriptions are publicly available.[†] The instrument simulator is implemented only in IDL. The operational software in python, created by E. Bustos and detailed below, depends on the specific hardware and is not freely distributed.

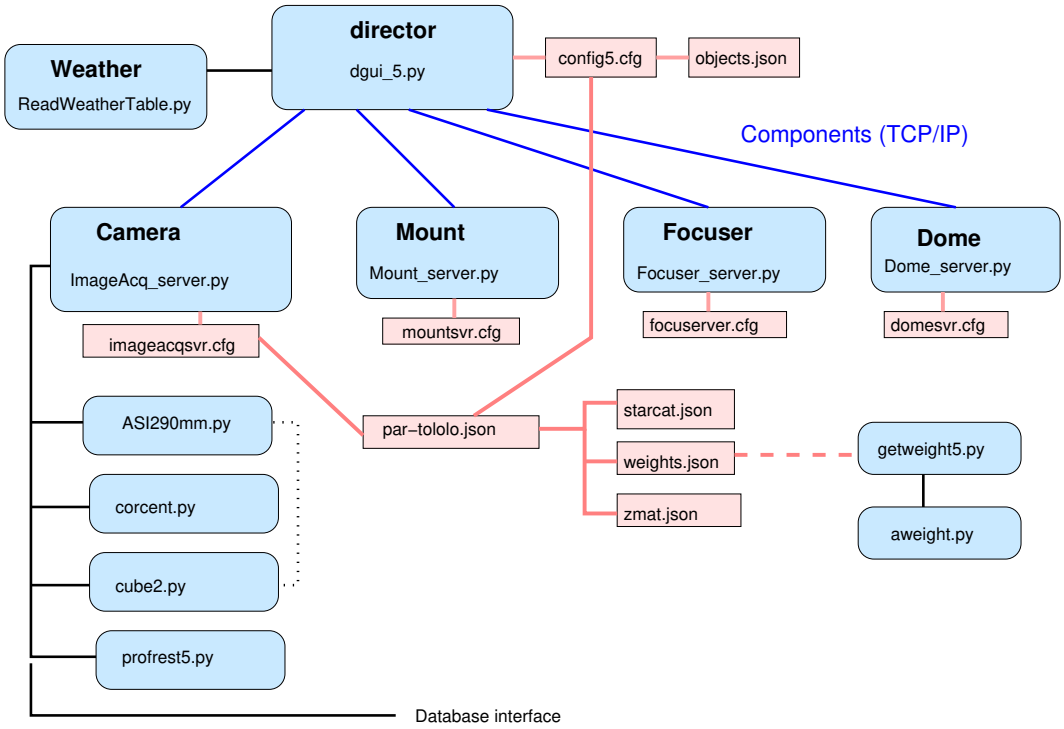

Figure 3. Main components of the RINGSS operational software. Blue boxes are software modules, pink boxes are configuration files.

Figure 3 illustrates the modular software architecture. Individual subsystems (camera, mount, etc.) are implemented as independent modules that can run on any computer. The system operation is controlled by the `director` module, connected to the components via TCP/IP sockets. Several configuration files (in the JASON format) specify the instrument and the software parameters. To avoid duplication of the same parameter (e.g. the pixel scale), the configuration files are cross-referenced, so this parameter is given only in one place (e.g. in `par-tololo.json`), and the name of this file is listed in other configurations where the pixel scale is needed.

The camera server uses the image acquisition module `ASI290mm.py`, which can also be run as a stand-alone GUI for manual operation. This module, included in the public distribution, utilizes the vendor-supplied camera driver (USB 3.0 interface). The camera server receives high-level commands. For example, *Snapshot* takes a wide-field image for pointing (its format and exposure time are defined in the configuration), finds the ring center by correlation using `corcent.py`, and returns it to the calling program, `director`. The latter centers the star iteratively by computing and applying mount offsets and repeating the snapshots. When the centering error is within tolerance, the command *Cubes* executes the measurement sequence. Ten 2000-frame (2-s) image cubes are taken sequentially. The cubes are processed immediately by `cube2.py` (not saved), and the results (statistical moments) are written to a text file with `.stm` extension. After completion of the 10-cube sequence, the average moments are used to derive the turbulence profile with `profrest5.py` and to write it to the `*.prof` file. The profile restoration can be repeated later off-line (e.g. with modified WFs) using either python or IDL codes. New results can be pushed to the database, if defined so the configuration.

[†]http://www.ctio.noirlab.edu/~atokovin/ringss/

The `director` module repeats the measurement sequence (with image re-centering and focus adjustment) until a change of star is needed (defined by the local sidereal time and the input star catalog). If the star disappears (clouds), pointing is repeated after a certain waiting period. Measurements are stopped and the dome is closed if the weather parameters (wind, humidity) exceed the thresholds or when the Sun altitude is above $-10°$ (end of the night).

3. FIRST RESULTS

3.1 Comparison with the MASS-DIMM at Cerro Tololo

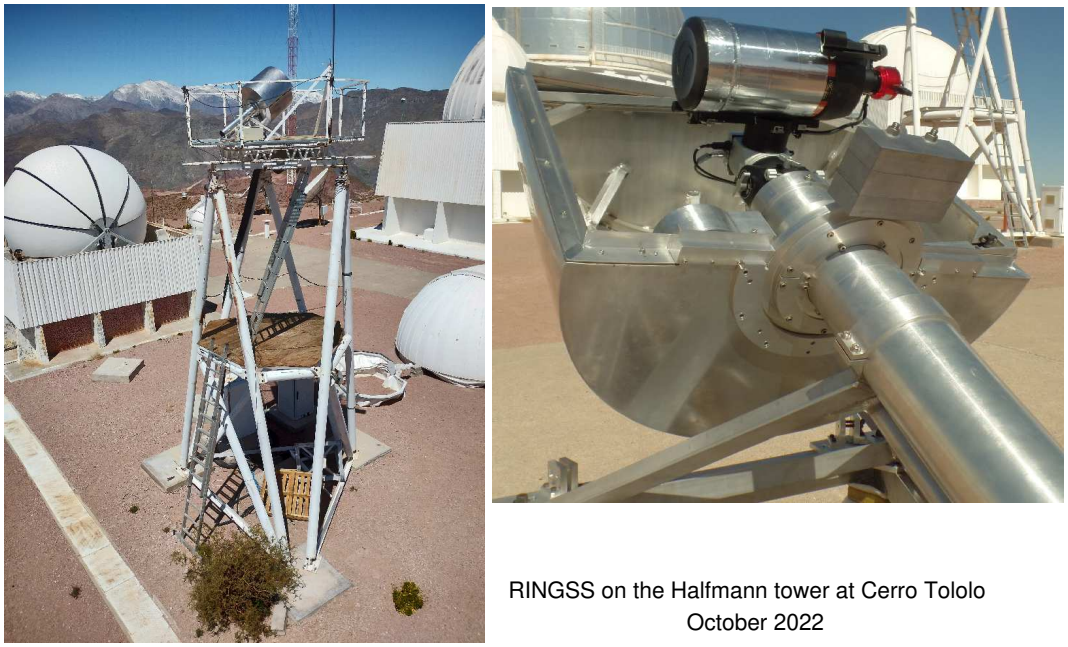

Figure 4. RINGSS-1 installed on the Halfmann tower at Cerro Tololo (left), and details of the cylindrical enclosure (right).

The first RINGSS instrument has been mounted in equatorial configuration in a custom-made cylindrical enclosure designed by R. Rivera (Fig. 4). The motor-driven upper half of the enclosure cylinder provides secure protection of the instrument in the closed state (tested during the snow storm in 2022 July) and a small cross-section to the wind when opened. The instrument has been installed at Cerro Tololo on the 6-m high Halfmann tower that hosted the TMT site monitor until 2012. After initial tests and adjustments, robotic operation started in 2022 November and continues now. The RINGSS-1 system provides an alternative to the aging regular MASS-DIMM site monitor located the adjacent tower.

Data from the MASS-DIMM and RINGSS monitors were collected and matched in time within 1 min, resulting in 18,901 measurements in common covering 58 nights. The Strehl ratios in DIMM were high, $\sim$0.8, and the spot separation was stable.

Overall, the seeing values measured by RINGSS and DIMM agree very well, the median seeing ratio RINGSS/DIMM is 1.02 (Fig. 5). Here and below, the seeing derived from the RINGSS turbulence profiles (scintillation-based) is used. One can note that RINGSS tends to measure a larger seeing than DIMM when it is poor and a better seeing when it is good. The formal linear regression is

$$\epsilon_{\rm RINGSS} = -0.274 + 1.355\epsilon_{\rm DIMM}. \quad (2)$$

This effect is clearly seen in the right-hand plot of Fig. 5: the seeing spikes in RINGSS are sharper and higher, while the samples 800-900 show that RINGSS measured a substantially better seeing than DIMM; at the same time, the RINGSS sector seeing was closer to DIMM. This so-called "good-seeing discrepancy" was investigated

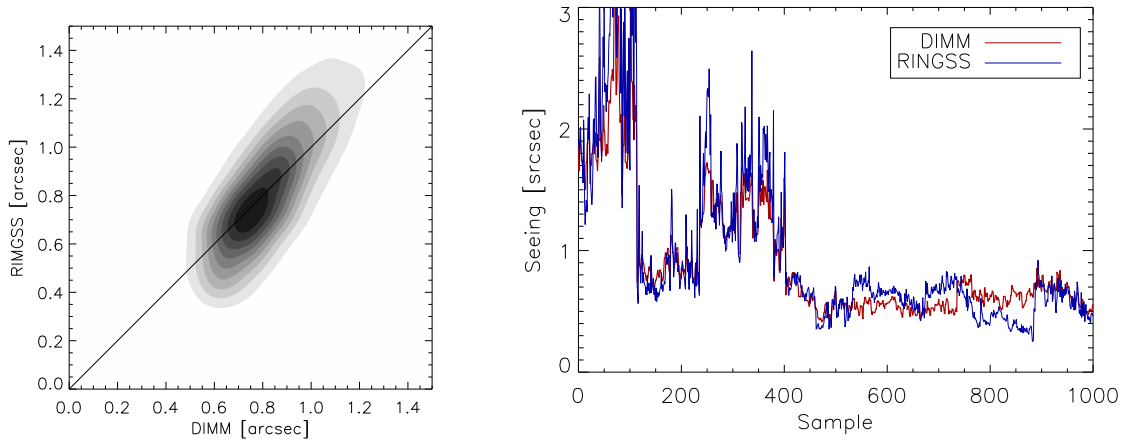

Figure 5. Comparison between total seeing measured by DIMM and RINGSS. Left: XY plot (line marks equality), right: evolution for the 1000 first time-matched points.

in detail. It occurs when the ground layer turbulence is weak and the good seeing is dominated by weak layers at high altitude. Simulations can reproduce the discrepancy between two RINGSS seeing estimates by assuming that the ring is not perfectly sharp (e.g. has additional spherical aberration). Considering that the real instrument has some residual chromatic aberration (indeed, the actual ring is 10% wider than diffraction-limited), this is a likely explanation. Simulations also show that the scintillation-based seeing is always closer to reality than the sector seeing, and this is why it is preferred here. Minor residual aberrations in the DIMM can play a similar role, biasing the results to larger values (see ref. 15). On the other hand, spikes of poor seeing caused by high layers can be under-estimated by the regular DIMM that uses the altitude-independent weight and does not correct for saturation. The two effects together would explain the non-unit slope in eq. 2.

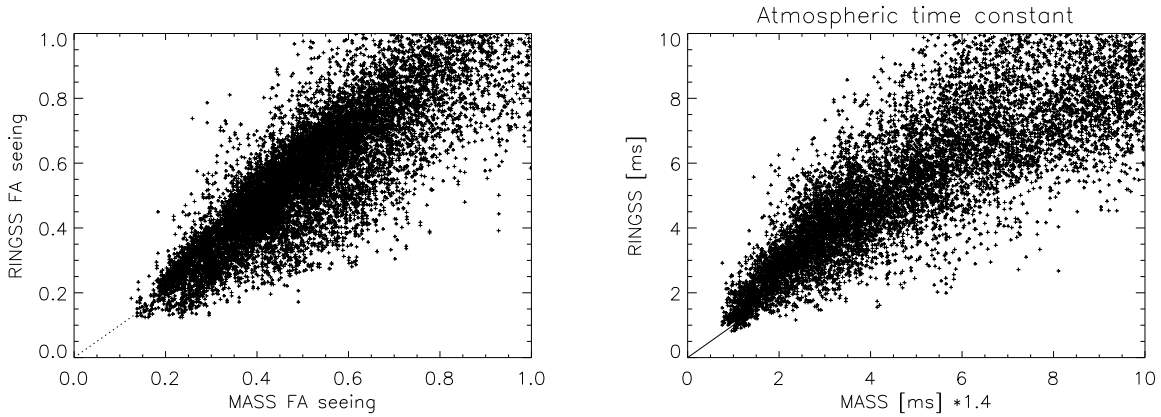

Figure 6. Comparison between MASS and RINGSS data products at Cerro Tolo: the free-atmosphere (FA) seeing (left) and the AO time constant τ_0 (right). In both plots, the diagonal line marks equality.

Figure 6 complements by comparing the MASS data products (free-atmosphere seeing and the AO time constant τ_0) with RINGSS. For RINGSS, the FA seeing is computed from the sum of turbulence integrals from 0.5 km up, adding half of the 0.25-km layer to better emulate MASS which does not have the 0.25-km layer. Both median and mean ratio of the FA seeing RINGSS/MASS is 1.11. As for the time constant, it is known that the method implemented in MASS is very approximate and its results are biased.[‡] The values of τ_0 reported by

[‡]Tokovinin, A. 2009. Calibration of the MASS time constant by simulation. http://www.ctio.noirlab.edu/~atokovin/profiler/timeconstnew.pdf

MASS with a corrective factor of 1.4 agree reasonably well with RINGSS.

3.2 The Paranal campaign

The second RINGSS instrument assembled by us participated in the turbulence profiling campaign at Paranal organized by ESO (February 28 to March 4, 2023). Full results of the campaign will be published jointly with other participants elsewhere. The portable turbulence profilers, RINGSS, SHIMM,[3] and FASS,[5] were installed close to each other on small piers or tripods, 1.5 to 2 m above ground. They were affected by a stronger ground-layer turbulence, compared to the regular Paranal site monitor, located on a 6-m tower a few hundred meters away. Of interest here is comparison of the RINGSS turbulence profiles with the results of the stereo-SCIDAR[11] that operated on a 1.8-m AT telescope. The SCIDAR observations were obtained by J. Velasquez and processed by T. Butterly using an improved algorithm.[2] RINGSS operated robotically with its mount in the alt-azimuth configuration.

The SCIDAR profiles have a vertical resolution of 250 m and an acquisition time of 2 min; contribution of the dome seeing is subtracted. The data of both instruments are $J_i = C_n^2(h_i)\mathrm{d}h$ integrals at a fixed-height grid h_i. SCIDAR and RINGSS operated from different locations, so comparison of the first (ground) layer is meaningless. The next two SCIDAR layers at 0.25 and 0.5 km match the RINGSS layers. Further up, the SCIDAR data were convolved with the notional RINGSS response in altitude, namely triangular functions in $\log H$ centered on the RINGSS layers at 1, 2, 4, 8, and 16 km with a full width of $\pm 2\times$. The response remains flat at $h > 16$ km.

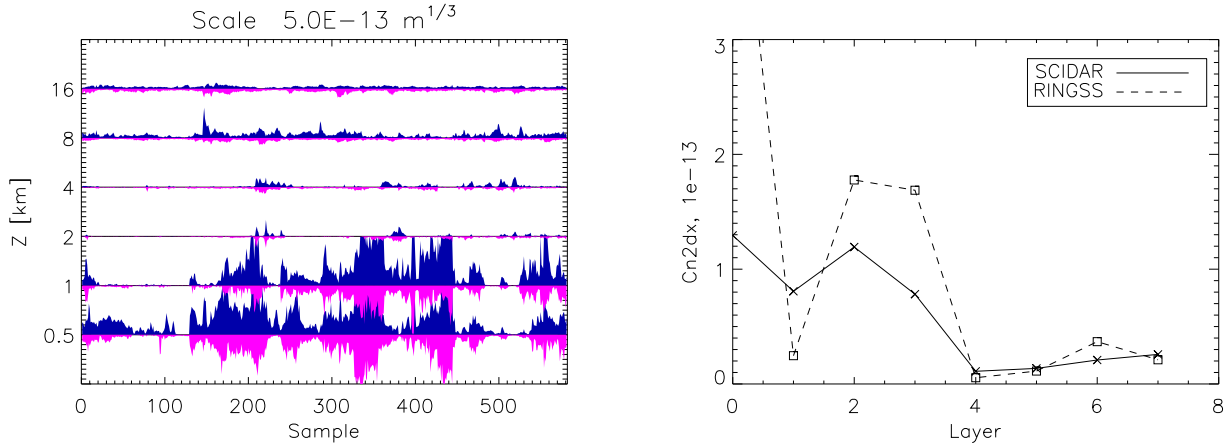

Figure 7. Comparison between RINGSS (up-facing blue bars) and SCIDAR (down-facing magenta bars) turbulence profiles matched in time and resolution (left) and between the mean profiles (right).

The 611 SCIDAR profiles matched in time within 2 min. with RINGSS are compared in Fig. 7. An excellent qualitative agreement is obvious. The two instruments were located at a certain distance and looked in different directions, so a detailed match is not expected. Indeed, some turbulence spikes occur at slightly different moments in time or with a different intensity. The right-hand panel compares the mean profiles. One notes that RINGSS under-estimates layer 1 at 0.25 km and over-estimates layers 2 and 3 (0.5 and 1 km). Tuning of the RINGSS profile restoration (e.g. extending the maximum fitted frequency from $m = 15$ to $m = 17$) seems to distribute the turbulence more evenly between layers 1 and 2, but this issue requires further investigation. Both instruments registered very weak turbulence in layers 4 and 5 (2 and 4 km) and some turbulence in the two upper layers.

Finally, Fig. 8 compares the effective wind speed V_2, used to estimate the AO time constant. It is measured by RINGSS with the Kornilov's method[9] and computed for SCIDAR as a turbulence-weighted mean V_2^2, ignoring the two lowest layers below 0.5 km:

$$V_2^2 = \sum_{i'} V_{i'}^2 J_{i'} / \sum_i J_i \tag{3}$$

where i is the layer number, V_i is the wind speed, and J_i is the turbulence integral in this layer. The first sum includes only the layers i' where the wind speed is measured by SCIDAR. The second sum (in the denominator)

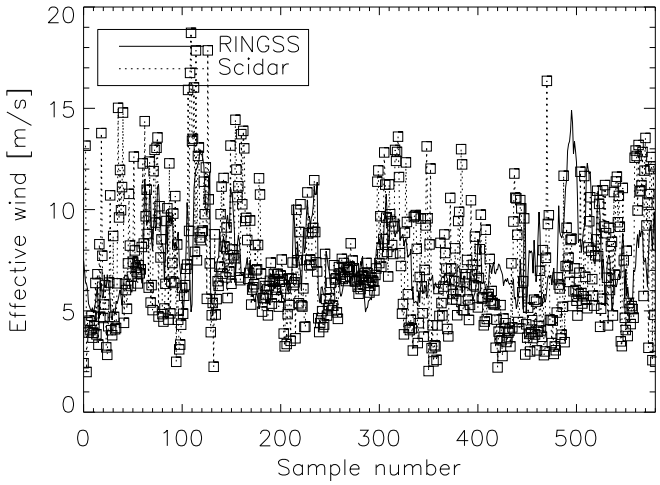

Figure 8. Effective wind speed V_2 measured by RINGSS and SCIDAR.

can include either all layers i or only the layers with measured wind speed i'. These two alternative estimates of V_2 from SCIDAR differ substantially between themselves and with the RINGSS wind speed: the first is smaller and the second is larger. However, the arithmetic mean of both estimates agrees with RINGSS quite well (this mean is plotted in Fig. 8 by squates and dotted line).

4. SUMMARY

The RINGSS method of measuring turbulence profiles from scintillation of single stars using a CMOS light detector[17] is a development of previous concepts, MASS and DIMM. It borrows the idea of angular power spectrum from FASS.[4] All these methods are based on the same theory and have been checked by simulation. In this sense, there is no doubt that their results can be trusted. One should keep in mind, however, that the turbulence intensity C_n^2 is parameter of a stationary random process that matches the reality only approximately, so the "exact" turbulence profile at a given location, time, and direction is a purely theoretical concept.

The RINGSS instrument that implements this idea has been built and tested, as reported above. Comparison with alternative turbulence profilers, MASS-DIMM and SCIDAR, indicates a satisfactory agreement. Upgrades of the obsolete MASS-DIMM systems to versions of RINGSS are recommended. Compared to MASS with its four detectors of lower quantum efficiency, RINGSS has a stronger and reacher input information (image pixels), hence better and more robust results. Operationally, the current RINGSS implementation benefits from its compactness, allowing a smaller enclosure and a better portability.

ACKNOWLEDGMENTS

The development of RINGSS was initiated by the NSF proposal to study sites in the continental US. Unfortunately, this program has not been pursued further. We thank the CTIO workshop for careful fabrication of the RINGSS-1 enclosure. We are grateful to the organizers of the Paranal campaign Miska Le Louarn and Angel Otarola for the generous support of the RINGSS team and efficient on-side help, to Jose Velasquez and Tim Butterly for observations with SCIDAR and their processing.

REFERENCES

[1] Avila, R., Vernin, J., Chun, M. R., and Sanchez, L. J. "Turbulence and wind profiling with generalized scidar at Cerro Pachon," *Proc. SPIE* **4007**, 721 (2000)

[2] Butterley, T., Sarazin, M., Le Louarn, M., Osborn, J., and Farley, O. J. D. "Correction of finite spatial and temporal sampling effects in stereo-SCIDAR". *Proc. SPIE* **11448**, *Adaptive Optics Systems VII*, 114481W (2020).

[3] Griffiths, R., Osborn, J., Farley, O., Butterley, T., Townson, M. J., and Wilson, R. "Demonstrating 24-hour continuous vertical monitoring of atmospheric optical turbulence", *Opt. Express* **31**, 6730 (2023)

[4] Guesalaga, A., Perera, S., Osborn, J., Sarazin, M., Neichel, B., and Wilson, R. "FASS: the full aperture seeing sensor," *Proc. SPIE* **9909**, id. 9909090H, 11 pp. (2016)

[5] Guesalaga, A., Ayancan, B., Sarazin, M. et al. "FASS: a turbulence profiler based on a fast, low-noise camera," *MNRAS* **501**, 3030–3045 (2020)

[6] Klückers, V. A., Wooder, N. J., Nicholls, T. W., Adcock, M., Munro, I., and Dainty, J., "Profiling of atmospheric turbulence strength and velocity using a generalised SCIDAR technique," *Astronomy & Astrophysics Supplement Series* **130**, 141–155 (1998)

[7] Kornilov, V., Tokovinin, A., Voziakova, O., Zaitsev, A., Shatsky, N., Potanin, S., and Sarazin, M. "MASS: a monitor of the vertical turbulence distribution," *Proc. SPIE* **4839**, 837 (2003)

[8] Kornilov, V., Tokovinin, A., Shatsky, N., Voziakova, O., Potanin, S., and Safonov, B. "Combined MASS-DIMM instrument for atmospheric turbulence studies," *MNRAS* **383**, 1268–1278 (2007)

[9] Kornilov, V. "Stellar scintillation in the short exposure regime and atmospheric coherence time evaluation," *Astronomy & Astrophyics* **530**, 56 (2011)

[10] Ogane, H., Akiyama, M., Oya, S., and Ono, Y. "Atmospheric turbulence profiling with multi-aperture scintillation of a Shack-Hartmann sensor," *MNRAS* **503**, 5778–5788 (2021)

[11] Osborn, J., Wilson, R. W., Sarazin, M. et al. "Optical turbulence profiling with Stereo-SCIDAR for VLT and ELT," *MNRAS* **478**, 8250 (2018)

[12] Potanin, S. A., Kornilov, M. V., Savvin, A. D. et al. "A Facility for the Study of Atmospheric Parameters Based on the Shack-Hartmann Sensor," *Astrophysical Bull.* **77**, 214–221 (2022).

[13] Robert, C., Conan, J.-M., Michau, V., Fusco, T., and Vedrenne, N. "Scintillation and phase anisoplanatism in Shack-Hartmann wavefront sensing," *JOSA(A)* **23**, 613–624 (2006)

[14] Schöck, M., Els, S., Riddle, R. et al. "Thirty Meter Telescope Site Testing I: Overview," *PASP* **121**, 384 (2009)

[15] Tokovinin, A. and Kornilov, V. "Accurate seeing measurements with MASS and DIMM," *MNRAS* **381**, 1179–1189 (2007)

[16] Tokovinin, A., Kellerer, A., and Coude Du Foresto, V. "FADE, an instrument to measure the atmospheric coherence time," *Asronomy & Astrophyics* **477**, 671–680 (2008)

[17] Tokovinin, A. "Measurement of turbulence profile from defocused ring images," *MNRAS* **502**, 794–808 (2021)